








## Controlling topological defect transitions in nanoscale lead zirconate titanate heterostructures

Vivasha Govinden <sup>1,\*</sup> Suyash Rijal <sup>2,\*</sup> Qi Zhang <sup>1,†</sup> Daniel Sando <sup>1</sup> Sergei Prokhorenko <sup>2,‡</sup> Youstra Nahas <sup>2</sup>  
Laurent Bellaiche <sup>2</sup> and Nagarajan Valanoor<sup>1,§</sup>

<sup>1</sup>*School of Materials Science and Engineering, University of New South Wales, Sydney, New South Wales 2052, Australia*

<sup>2</sup>*Physics Department and Institute for Nanoscience and Engineering, University of Arkansas, Fayetteville, Arkansas 72701, USA*



(Received 5 September 2021; accepted 8 November 2021; published 15 December 2021)

Varying thickness in ferroelectric heterostructures systematically changes both the strain and the electrical boundary conditions and thus the polarization screening. This has a direct result on the observed ferroelectric nanotopologies, from polar vortices, skyrmions, and bubbles to Kittel type stripe/labyrinthine domains. Here, a control of the topological defect transitions is reported in epitaxial (001)-oriented  $\text{PbZr}_{0.4}\text{Ti}_{0.6}\text{O}_3/\text{SrTiO}_3/\text{PbZr}_{0.4}\text{Ti}_{0.6}\text{O}_3$  (PZT/STO/PZT) heterostructures. Piezoresponse force microscopy is exploited to capture various topological defect states, such as merons, skyrmions, dislocations, bimerons, and three- or fourfold junctions and hence to understand their transition pathways. The thickness of the dielectric spacer and/or ferroelectric layer is tuned during growth to manipulate the strength of the residual depolarization field; this consequently leads to a range of the abovementioned topological defect structures. This is further corroborated by effective Hamiltonian-based Monte Carlo simulations that provide insight into why and how altering the thickness of ferroelectric or dielectric layers triggers topological phase transitions. This controlled design of nanoscale ferroic topologies opens possibilities of engineering emergent transitions.

DOI: [10.1103/PhysRevMaterials.5.124205](https://doi.org/10.1103/PhysRevMaterials.5.124205)

### I. INTRODUCTION

Nanoscale ferroelectric topological structures [1] have recently garnered immense interest. Researchers have demonstrated the existence of exotic topological configurations such as vortices [2–4], vortex pairs [2,5–7], flux-closure [8–11], polar skyrmions [2,12–14], dipolar waves [15,16], nanoscale bubble domains [17,18], merons [19], bimerons [14], three- or fourfold junctions [20], and hedgehogs [21–23]. A few examples of functionalities associated with these topological structures are nonlinear optical response [24], chirality [25,26], giant electromechanical response [17], negative capacitance [27], and enhanced electrical conductivity [28]. It is now recognized that such ferroelectric topologies are stabilized by imposing specific mechanical and electrical boundary conditions [21,29].

Mechanical boundary conditions refer to the film strain conditions, including epitaxial strain imposed by the substrate upon an epitaxial thin film. They can be manipulated either by changing film thickness [30] or by using substrates with different lattice parameters [31]. In addition, strain gradients in films with large misfit strains are reported to induce flexoelectricity [32–37], thus favoring polarization rotation in the ferroelectric film. This stabilizes [14] those topologies which possess a curl of the order parameter [10], i.e., bubbles, flux-closures, vortex [2,11], antivortex, and center type domains.

On the other hand, electrical boundary conditions depend on the extent of screening of bound charges at interfaces. However, a real electrode fails to provide 100% screening due to its limited screening lengths [38,39], and this incomplete screening of ferroelectric bound charges causes a depolarization field [40].

It was recently found that electrical boundary conditions can also be engineered by introducing a dielectric spacer in between two ferroelectric layers [41,42]. It is, however, not clear how modifying the thickness of the dielectric spacer affects the morphology of the topological state because of two competing mechanisms. One mechanism originates from the realization that short-period superlattices made of ferroelectric and dielectric materials can give rise to monodomainlike states (i.e., states that are close to short-circuit-like conditions), while longer-period superlattices made of exactly the same compounds generate stripe patterns (i.e., states that are close to open-circuit-like conditions) [43]. This is because short-period systems behave as a “new single material,” while longer-period systems behave as two separate entities. Adopting this view, one may thus consider that shortening the spacer thickness will push the system to adopt short-circuit-like topological states. However, there is a second competing mechanism at play: when decreasing the thickness of the dielectric space layer, there will be fewer carriers to screen the polarizing-induced surface charges at the ferroelectric/dielectric interface. The depolarization field can thus increase, and the adopted topological phase becomes closer to open-circuit-like conditions.

Moreover, it is a challenge to predict which topological phase is most likely to occur upon ferroelectric layer thickness reduction. As a matter of fact, two different ef-

\*These authors contributed equally to this work.

†peggy.zhang@unsw.edu.au

‡sprokhor@uark.edu

§nagarajan@unsw.edu.au

fects can compete. One stems from the fact that, when the thickness decreases, the ratio between surface and inner dipoles increases. Consequently, it may be easier to transition to topological states that are closer to short-circuit-like conditions since surface dipoles have the tendency to align in plane (to form flux-closure configurations) and thus effectively screen the depolarizing field felt by inner dipoles. On the other hand, the second consideration is that, typically, a decrease in thickness is accompanied by an increase in the depolarizing field [44] because, e.g., there are fewer carriers to screen the polarizing-induced surface charges. This second mechanism may thus favor states that are closer to open-circuit-like conditions.

In previous work, we exploited the spacer approach to realize as-grown nanoscale bubble [14,17] and labyrinthine domains [14,45] in two separate systems with dielectric spacers sandwiched between ferroelectric layers. These labyrinthine domains are stabilized as the branching of the domain walls increases the entropy [20] and effectively reduces the gradient polarization energy [46]. We also presented phase diagrams which outlined the stability of (1) bubble vs labyrinthine domains as a function of screening [17] and (2) monodomain vs labyrinthine as well as transitional topological defects as a function of temperature and electric field [14]. More precisely, Nahas *et al.* [14] showed that PZT films with a fixed thickness and under some fixed strain conditions adopt different topological phases when progressively increasing an electric field. The phases result in the following order: connected labyrinths, disconnected labyrinths, mixed bimeron-bubble phases, skyrmion/bubble phases, and monodomains. The increase in electric field alters the residual depolarization field, causing a transition from open-circuit-like to short-circuit-like conditions. This was experimentally achieved by applying a DC bias to the scanning probe microscopy tip [14,24]. Hence, these topological transitions have been triggered in an *ex situ* manner (via temperature or electric field), and this begs the question: can topological transitions rather be controlled during synthesis of epitaxial heterostructures?

Our model system is an ultrathin (001)-oriented  $\text{PbZr}_{0.4}\text{Ti}_{0.6}\text{O}_3/\text{SrTiO}_3/\text{PbZr}_{0.4}\text{Ti}_{0.6}\text{O}_3$  (PZT/STO/PZT) heterostructure fabricated on a  $\text{La}_{0.67}\text{Sr}_{0.33}\text{MnO}_3$  (LSMO)-buffered STO substrate. In these PZT sandwich films, changing the thickness of the different layers triggers a transition from labyrinthine to nanoscale bubble domains. Labyrinthine domains were observed in PZT (9 nm)/STO (3 u.c.)/PZT (9 nm)/LSMO (40 nm)//STO substrate. With a decrease in STO spacer thickness (to 2 u.c.), the poled up labyrinthine domains become finer. A reduction in the PZT thickness results in the breakdown of these labyrinthine domains into a mixture of disjointed and nanoscale bubble domains. Closer inspection of the disjointed domains using high-resolution piezoresponse force microscopy (PFM) reveals a rich tapestry of transitional topological defect states. We report the occurrence of several topological defects such as merons, skyrmions, dislocations, bimerons, and three- or fourfold junctions. Additional investigation using the avenue of Monte Carlo simulations based on the effective Hamiltonian [29,47,48] confirms and explains such experimental findings, namely: (1) owing to the enhancement of interface effects, a decrease in thickness of ferroelectric

layers facilitates the transition toward short-circuit-like topological states; and (2) a decrease in thickness of dielectric layers can be understood in terms of decrease in the magnitude of the depolarization field, which also triggers transitions toward short-circuit-like topological states. The comprehensive study in this paper demonstrates that the precise manipulation of thickness of ferroelectric and dielectric layers can be a powerful method to systematically achieve deterministic control of the topological defects appearing in such modulated phases.

## II. METHODS

### A. Experimental details

Here, (001)-oriented PZT/STO/PZT sandwich films were grown on (001) etched stepped STO substrates (Shinkosha, Japan) with an LSMO bottom electrode, using a pulsed laser deposition (PLD) system (Neocera, USA). An ultraviolet excimer laser beam (COMPex PRO 102, Coherent, Germany) with a wavelength of 248 nm was used. PZT was chosen due to its large lattice mismatch with the STO substrate. This leads to partially relaxed PZT films, with a compressive strain gradient.

The thickness of each individual layer (ferroelectric layer, bottom electrode, and the dielectric spacer) was controlled by tuning the effective incident laser energy [49] while keeping the number of pulses constant. Here, effective laser energy refers to the energy ablating the target [50], which was measured before deposition from inside the PLD chamber using a Laser Power and Energy Meter (FieldMasterTM, Coherent, Germany). This allowed us to exclude dissipation across lenses and mirrors [49] along the beam path.

The deposition temperature for the LSMO layer was maintained at 800 °C and lowered to 700 °C for the PZT and STO layers. During ablation, the oxygen pressure was kept at 100 mTorr for LSMO, 50 mTorr for PZT, and reduced to 20 mTorr for STO. After deposition, the films were cooled to room temperature at a rate of 20 °C/min in an oxygen atmosphere of 450 Torr.

X-ray diffraction (XRD) was conducted on the samples, where  $\theta$ - $2\theta$  XRD patterns were obtained on a SmartLab Intelligent XRD System (Rigaku, Japan), and reciprocal space maps (RSMs) were acquired on a PHILIPS X'Pert PRO Materials Research Diffraction system (Panalytical Pty, Netherlands). The  $\theta$ - $2\theta$  pattern of each film was fitted using a custom-made MATLAB fitting program [51] to estimate the thickness of each individual layer. This fitting program generates simulated  $\theta$ - $2\theta$  patterns based on calculations using Bragg's law of reflection, the atomic scattering, and structure factors of each constituting element. The fitting details are given in the Supplemental Material (S1) [52]. The thickness of the LSMO layer was maintained at  $37 \pm 3$  nm for all samples. Within this narrow range, the change in carrier density is minimal, and hence, screening provided by the LSMO layer can be assumed to be constant for all samples [53].

Surface topography and ferroelectric domains were imaged with a commercial atomic force microscopy (AFM) system (Cypher S, Asylum Research, US) using the dual AC resonance tracking (DART) PFM mode. During scanning, an AC

TABLE I. Composition and thickness of each sample.

Sample name	Sample configuration	Detailed layer by layer composition of sample
F1	S3-PZT9	PZT(9 nm)/STO(3 u.c.)/PZT(9 nm)/LSMO//STO substrate
F2	S2-PZT9	PZT(9 nm)/STO(2 u.c.)/PZT(9 nm)/LSMO//STO substrate
F3	S2-PZT8	PZT(8 nm)/STO(2 u.c.)/PZT(8 nm)/LSMO//STO substrate

bias of 0.3 V at  $\sim 350$  kHz was applied to the Pt/Cr-coated conductive AFM probes (ElectriMulti 75G, BudgetSensors, Bulgaria) which have an average radius of  $<25$  nm.

### B. Numerical details

We performed Monte Carlo simulation based on the effective Hamiltonian [29] in which the total energy has the form

$$\begin{aligned} \varepsilon_{\text{tot}}(\{\mathbf{u}_i\}, \{\sigma_i\}, \{\mathbf{v}_i\}, \eta) = & \varepsilon_{\text{Heff}}(\{\mathbf{u}_i\}, \{\sigma_i\}, \{\mathbf{v}_i\}, \eta) \\ & + \beta_s \sum_i \langle \mathbf{E}_{\text{dep}} \rangle \cdot Z^* \mathbf{u}_i - \sum_i \mathbf{E} \cdot Z^* \mathbf{u}_i, \end{aligned} \quad (1)$$

where  $\mathbf{u}_i$  is the local soft mode in the  $i$ th unit cell of the film, and the product of  $\mathbf{u}_i$  with the effective charge  $Z^*$  is the local electric dipole in this cell. Here,  $\sigma_i$  characterizes the atomic distribution of the B-site sublattice, where  $\sigma_i = 1$  ( $\sigma_i = -1$ ) implies the B-site is occupied by a Ti (Zr) atom. Variables  $\{\mathbf{v}_i\}$  are related to inhomogeneous strain inside the film, and  $\eta$  is the homogeneous strain tensor. The first term  $\varepsilon_{\text{Heff}}$  is the alloy effective Hamiltonian, i.e., intrinsic energy of the ferroelectric film [47], where the treatment of dipole-dipole interaction [48] leads to the maximum depolarization field ( $\langle \mathbf{E}_{\text{dep}} \rangle$ ). The second term  $\beta_s \sum_i \langle \mathbf{E}_{\text{dep}} \rangle \cdot Z^* \mathbf{u}_i$  represents screening of the depolarization field by a factor  $\beta_s$  (screening parameter). The final depolarization field that results as a combination of the first and second terms is thus given by  $(1 - \beta_s) \mathbf{E}_{\text{dep}}$ . Hence,  $\beta_s = 1$  represents the ideal short-circuit condition with no depolarization field, and  $\beta_s = 0$  represents the ideal open-circuit condition. The third term represents energy contribution by external electric field.

## III. RESULTS AND DISCUSSION

### A. Experimental observations

The results presented here focus on three PZT/STO/PZT sandwich films, the details of which are summarized in Table I. The thicknesses of each individual layer of the films were estimated by fitting their  $\theta$ - $2\theta$  patterns using a custom-made MATLAB program; the details are given in the Methods.

Figure 1(a) shows the XRD  $\theta$ - $2\theta$  scans of all PZT sandwich samples. The presence of only  $(0\ 0\ l)$  peaks (corresponding to the PZT and LSMO films as well as the STO substrate) confirms the absence of any misorientations and secondary phases. The in-plane strain state of each film was studied by analyzing the asymmetrical  $(103)$  RSMs, as shown in Figs. 1(d) and 1(f). The alignment of crystal truncation rods (CTRs) for LSMO and the STO substrate along  $Q_x$  attests that LSMO grows pseudomorphically on STO, attributed to the small lattice mismatch of 0.75%. For PZT layers, their

CTRs are all presented at lower  $Q_x$  values, indicating strain relaxation in the PZT layers. This is a result of a much higher theoretical misfit between PZT and STO, 1.92% (bulk lattice parameter  $a$  of PZT to be  $3.98$  Å) [54].

The out-of-plane lattice parameters for both PZT and LSMO layers were extracted from the  $\theta$ - $2\theta$  plots. Table II lists the out-of-plane and in-plane lattice parameters of all samples based on the asymmetrical RSM results [Figs. 1(d) and 1(f)], as well as the out-of-plane lattice parameters from the fittings. In each case, the out-of-plane parameter for the PZT layer ( $c = 4.130 \pm 0.004$  Å) is significantly larger than the in-plane parameter ( $a = 4.032 \pm 0.007$  Å). This implies all films are  $c$ -axis oriented with a net overall out-of-plane polarization.

The contrast in the strain state between the LSMO and PZT layers was further investigated by Williamson-Hall (W-H) plots [Fig. 1(b)]. The following equation was used:

$$\beta \cos \theta = \frac{K\lambda}{D} + 4\varepsilon_l \sin \theta, \quad (2)$$

where  $\beta = \beta_{\text{measured}} - \beta_{\text{instrument}}$ ,  $\beta_{\text{measured}}$  is the measured line width of film peaks,  $\beta_{\text{instrument}}$  is estimated from the line width of substrate peak,  $\theta$  is the Bragg angle,  $\lambda$  is the x-ray wavelength ( $1.5406$  Å; Cu  $K_\alpha$ ),  $K$  is a geometrical constant taken to be 1,  $D$  gives the coherence length along the scattering vector, and  $\varepsilon_l$  gives inhomogeneous strain. The slopes of the W-H plots ( $\beta \cos \theta$  vs  $4 \sin \theta$ ) thus give a measure of the inhomogeneous strain, i.e., strain gradient of the films.

As a representative case of this analysis, we present here the results for the sample S3-PZT9 (F1) as shown in Fig. 1(b). The slope for PZT is greater than that of LSMO, implying that PZT has a larger strain gradient than LSMO. Such slopes have been calculated for each sample and plotted in Fig. 1(c). The average strain gradient is relatively constant for all samples, at a value of  $0.15 \pm 0.02\%$  for the PZT layer and negligibly zero for the LSMO layer. These similar strain conditions for each sample, together with consistent lattice parameters obtained from RSMs, collectively indicate uniform mechanical boundary conditions for all samples. Also, a comparison between the strain gradient values and the RSM plots suggests that the contrast in the inhomogeneous strain values between the LSMO and PZT layers can be ascribed to film relaxation mechanisms [55], i.e., the LSMO is pseudomorphic, and the PZT layer is partially relaxed.

Next, we discuss the results of high-resolution DART PFM, as shown in Fig. 2, to investigate how the domain patterns change with film configuration. In the phase images, dark purple and yellow regions indicate poled up and down domains, respectively. The PFM data show a systematic change in the domain configuration (both amplitude and corresponding phase) as a function of samples with decreasing thickness of either dielectric spacer or PZT layer. As it was

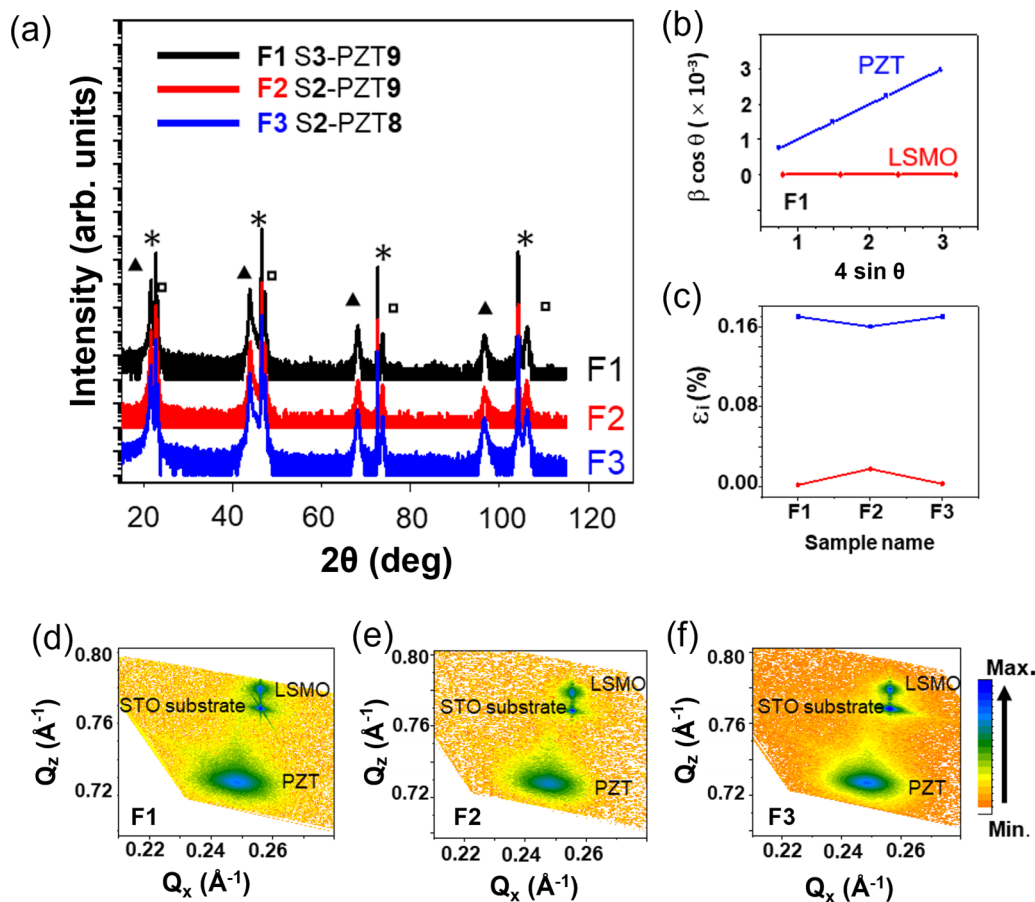


FIG. 1. (a)  $\theta$ - $2\theta$  scans showing (001)–(004) reflections of all samples ( $\square$  for LSMO peak,  $\blacktriangle$  for PZT peak, and  $*$  for substrate STO peak). (b) Out-of-plane Williamson-Hall (W-H) plots for PZT and LSMO films of sample S3-PZT9 (F1). (c) Variation in inhomogeneous strain (obtained from slopes of W-H plots) in both PZT and LSMO layers for the three samples. (d)–(f) Asymmetrical reciprocal space maps (RSMs) about (103) peak for samples F1–F3, respectively.

previously ascertained that the mechanical boundary conditions for all samples remain constant, these variations likely originate from changes in the electrical boundary conditions.

In sample F1 (S3-PZT9), labyrinthine structures with equal upward and downward polarization are observed [Figs. 2(a) and 2(d)]. Such labyrinthine domains form to minimize the extra energy cost associated with the depolarization field [56]. On average, the labyrinthine domains are  $>500$  nm in length with a width of  $\sim 50$  nm. When the STO spacer thickness is reduced from 3 to 2 u.c. (while keeping the thickness of the ferroelectric layer constant), the downward labyrinthine domains (yellow contrast) coarsen [Figs. 2(b) and 2(e)]. This

could result from the change in the dipolar coupling strengths between the individual PZT layers as the dielectric spacer thickness decreases [42]. Note that, given that the dead layer in LSMO is only a few unit cells thick [57], a small variation in LSMO thickness in the range of  $37 \pm 3$  nm should not play a significant role. The reduction in STO spacer thickness causes the labyrinthine domains with upward polarization (purple contrast) to break down into (i) smaller labyrinthine domains [white boxes in Figs. 2(b) and 2(e)] and (ii) disjointed nanoscale topological defect structures, discussed later in Fig. 3. The former smaller labyrinthine domains are 210 nm long on average, with a mean width of 40 nm, while

TABLE II. Out-of-plane and in-plane lattice parameters of PZT and LSMO layers for each sample. For the out-of-plane lattice parameter, the corresponding simulated values are also presented.

Sample name		Out-of-plane lattice parameter ( $\text{\AA}$ )				In-plane lattice parameter ( $\text{\AA}$ )	
		LSMO		PZT		LSMO	PZT
		Experimental	Simulated	Experimental	Simulated	Experimental	Experimental
F1	S3-PZT9	$3.852 \pm 0.004$	3.852	$4.130 \pm 0.004$	4.137	$3.903 \pm 0.004$	$4.027 \pm 0.004$
F2	S2-PZT9	$3.854 \pm 0.004$	3.854	$4.130 \pm 0.004$	4.132	$3.904 \pm 0.004$	$4.038 \pm 0.004$
F3	S2-PZT8	$3.852 \pm 0.004$	3.848	$4.130 \pm 0.004$	4.132	$3.903 \pm 0.004$	$4.025 \pm 0.004$

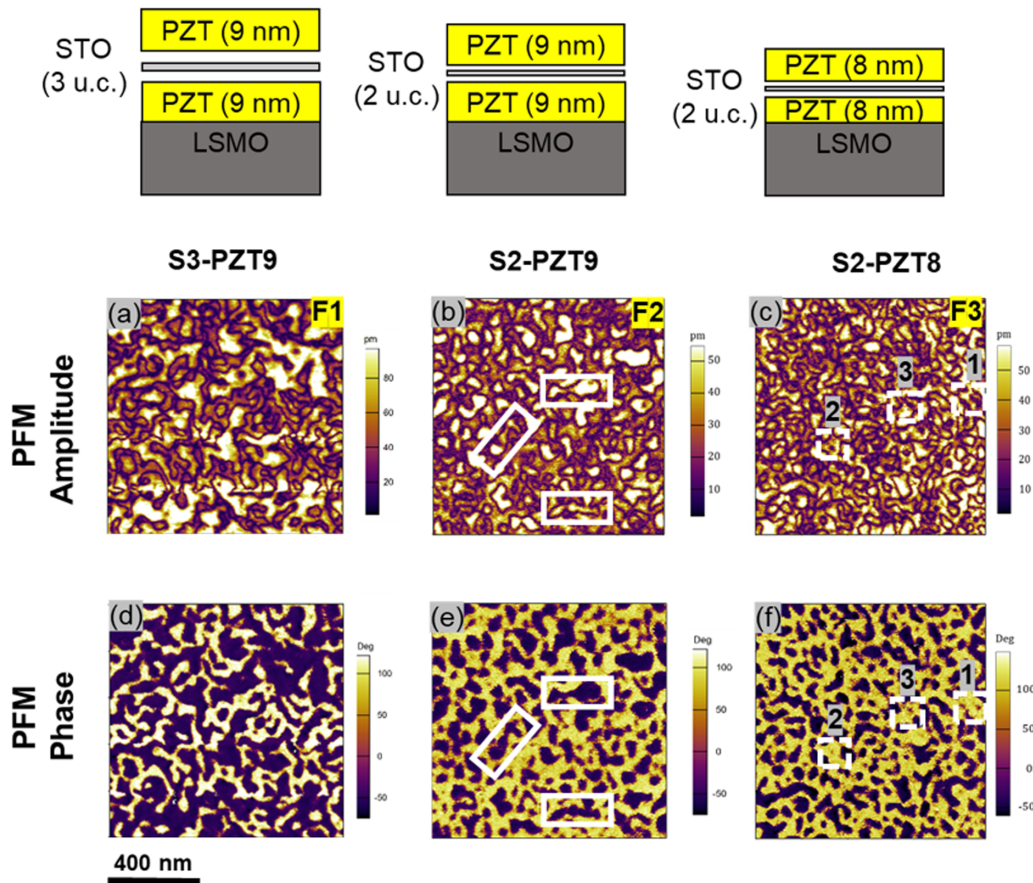


FIG. 2. (a)–(c) Piezoresponse force microscopy (PFM) amplitude and (d)–(f) PFM phase images illustrate ferroelectric domain evolution across the trend.

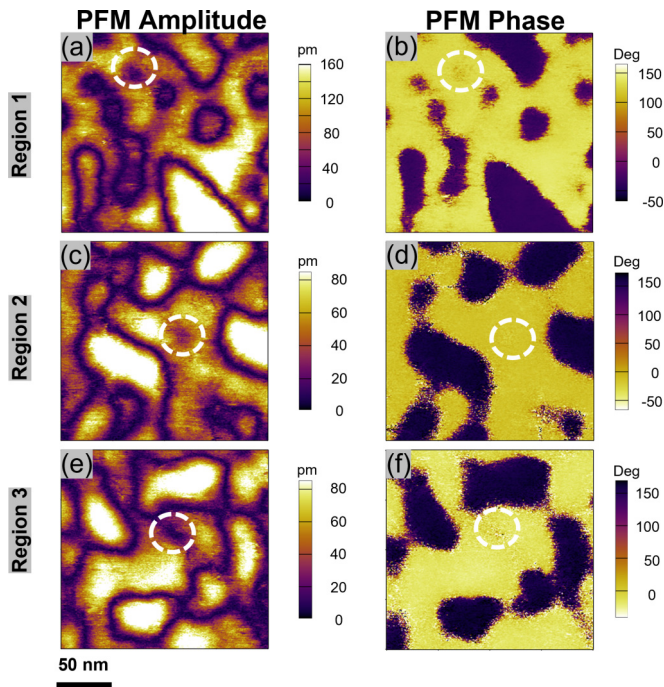


FIG. 3. (a), (c), and (e) Piezoresponse force microscopy (PFM) amplitude and (b), (d), and (f) phase images of S2-PZT8 (F3 sample) with white dotted circles depicting the occurrence of topological structure and nanoscale bubble domains. These  $200 \times 200$  nm images correspond to the white dotted squares in Figs. 2(c) and 2(f).

the latter disjointed domain diameter ranges from 20 to 70 nm. One could argue that such smaller labyrinths and disjointed structures are transitional domains that have been “frozen in,” as discussed in Nahas *et al.* [14]. In this latter work, disconnected labyrinths were found to be in intermediate state in the labyrinths to the bubble/skyrmion path, triggered by varying the external electric field. Here, we trigger a similar transition in as-grown films but by controlling the layer thicknesses.

When the thickness of the PZT layer decreases, the finer upward labyrinths break down into disjointed nanoscale morphologies as the depolarization field [40] is intensified. This leads to further changes in the ferroelectric topologies, as exemplified in PFM amplitude and phase images for film F3 (S2-PZT8) in Figs. 2(c) and 2(f). Compared with F2, the F3 sample exhibits a significantly finer domain size configuration with a smaller mean width of 30 nm and an extended length to 300 nm. Also, the diameter of the disjointed domains varies from 10 to 50 nm only.

The above domain transition also demonstrates the occurrence of hyperfine structures amid the disjointed domains, as shown within the white dotted squares in Figs. 2(c) and 2(f). Magnified  $200 \times 200$  nm PFM scans of F3(S2-PZT8) (Fig. 3) corresponding to the regions bound by the white squares in Figs. 2(c) and 2(f) reveal the existence of sub-10 nm domains (refer to the white dotted circles in Fig. 3). These nanodomains show blurry amplitude contrast and a faint upward domain phase of the domain wall. Previously,

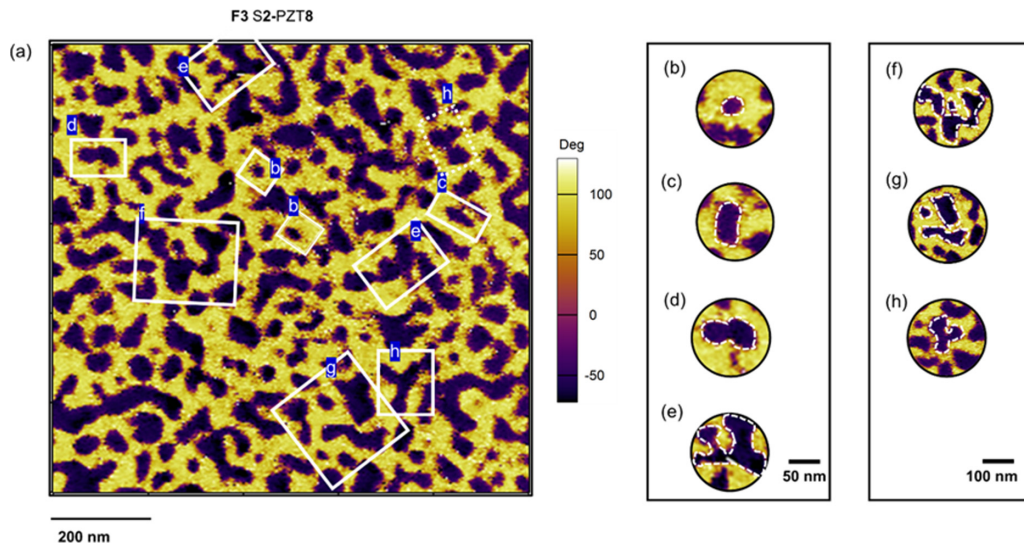


FIG. 4. (a) Piezoresponse force microscopy (PFM) phase images of S2-PZT8 (F3) with labels (b)–(h) corresponding to various topological defects. Digitally magnified PFM of the topological defects, namely, (b) skyrmion, (c) convex disclination (meron), (d) bimeron (elongated skyrmion or superposition of two convex disclinations), (e) saddle (fourfold junction), (f) handle (pair of nearby concave and convex disclinations), (g) dislocation, and (h) concave disclination (threefold junction). The white dotted contours serve as a visual aid to reveal the shape. These images correspond to PFM phase images excerpts from (a) and Fig. S2 in the Supplemental Material [52].

such features were ascribed to the presence of bubble domains, i.e., nanoscale ferroelectric topological structures with polarization rotation that leads to mixed Néel-Bloch walls [17]. In contrast, conventional  $180^\circ$  domains show sharp domain walls in PFM amplitude and  $180^\circ$  phase difference in the phase images, as depicted in Fig. 3.

So far, we have demonstrated a controlled evolution from labyrinthine to nanoscale bubble morphologies. This transition occurs through a series of intermediary topological defect states, as exhibited in Fig. 4. Here, several topological features have been observed and highlighted, namely, (i) skyrmion, (ii) meron [58], (iii) bimeron, (iv) saddle, (v) handle, (vi) dislocation, and (vii) threefold junction, as shown in Figs. 4(b)–4(h), respectively (see the Supplemental Material (S2) for a phase image of sample F2 (S2-PZT9) [52]). These topological defects, predicted by Nahas *et al.* [14], have been observed only in films, subject to external stimuli such as electric field and heat. Fig. 4 demonstrates that both thicknesses of the ferroelectric layer and spacer can be tuned to also stabilize these topological defects in as-grown films at the fabrication stage.

### B. Theoretical model

Figure 2 depicts that an interplay between thicknesses of the STO spacer and PZT thin films results in a range of dipolar patterns. Computationally, we approach this problem by decoupling the control parameters, namely, the thickness of PZT thin films and the screening parameter ( $\beta_s$ ), and studying their effects on polar topologies separately under an external electric field. This electric field will also tell us if, when changing the thickness, it is easier or more difficult (i.e., smaller or larger critical electric field) for the system to transform into short-circuit-like topological states. Moreover, one typically needs an applied electric field in the simulations

to also mimic the intensity of built-in bias or asymmetry in the experimental structure. We employ Monte Carlo simulation using the Metropolis algorithm, where we quench the system under  $-2\%$  compressive epitaxial strain from 2000 K down to two different temperatures, namely, 300 and 10 K (see the Supplemental Material (S3) [52]) and perform subsequently calculation with  $\beta_s$  and PZT thickness variation. Quenched structures were obtained by using an initial value of  $\beta_s = 0.6$ , when studying the effect of electrical boundary conditions. On the other hand, for the investigation of the effects of varying thickness, a constant value of  $\beta_s = 0.8$  is considered for all thicknesses.

We varied  $\beta_s$  on dipolar structures while keeping the external electric field constant in a fixed (i.e., the same thickness)  $56 \times 56 \times 5$  PZT supercell with periodic boundary conditions along pseudocubic [100] and [010] directions to understand the consequence of changing spacer thickness on a dipolar structure. An external electric field of magnitude  $30 \times 10^7$  V/m was applied along the [001] pseudocubic direction. At 300 K, upon changing  $\beta_s$ , varying dipolar structures were found, as shown in Figs. 5(c1)–5(c6). One notices the progressive change from connected labyrinths, disconnected labyrinths, bubble phase, and monodomain as  $\beta_s$  increases or, equivalently, when the depolarization field weakens. Hence, we can ascribe the breakdown of labyrinths into smaller domains observed in experiments when the spacer thickness decreases (Fig. 2) to a reduction in overall depolarization field. Such a decrease is attributed to the fact that short-period superlattices made of ferroelectric and dielectric layers have the tendency to behave as a new system rather than two separate components and therefore wish to form short-circuit-like states [43]. An example of how Figs. 5(b1)–5(b6) can be replicated in experiments is shown in the Supplemental Material (S4) [52], in which we investigate domain transitions when only the ferroelectric layer thickness varies. Table III

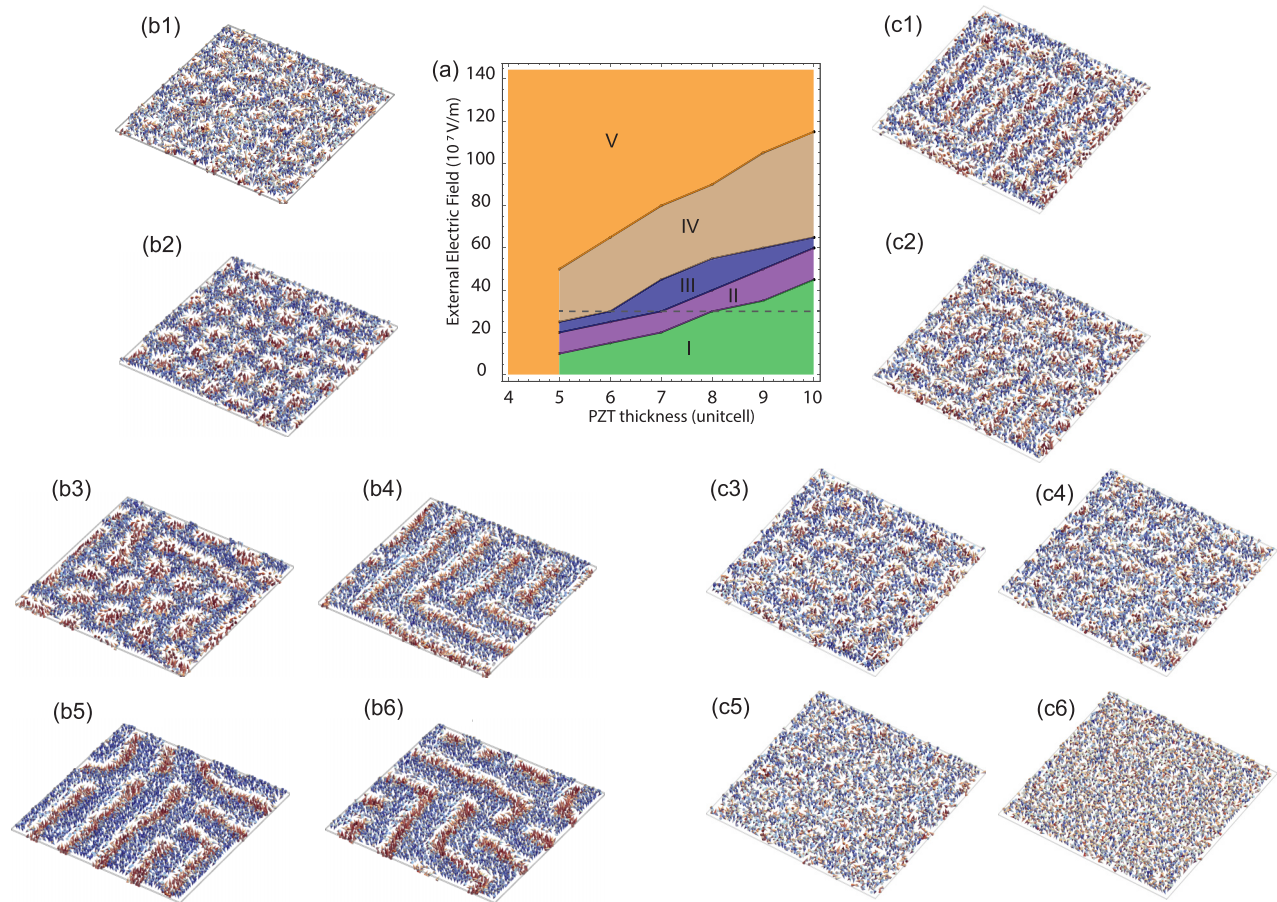


FIG. 5. (a) External electric field vs PZT thickness phase diagram at 300 K and  $\beta_s = 0.8$  (note that only integer PZT thicknesses are meaningful, and colors are a guide to the eye). Applied electric field is along the [001] pseudocubic direction. Phases I and II, respectively, correspond to connected and disconnected labyrinth patterns; phases III and IV represent a mixed bimeron-bubble phase and bubble phase, respectively; phase V denotes a monodomain phase where all dipoles are aligned with applied field. Dashed horizontal line emphasizes different possible phases for different thicknesses at a given electric field. (b1)–(b6) At 300 K, snapshots as generated by Monte Carlo simulations of a middle plane of  $56 \times 56 \times Z$  PZT supercells under  $30 \times 10^7$  V/m, where  $Z$  is film thickness increasing from 5 to 10 layers. (c1)–(c6) At 300 K, snapshots as generated by Monte Carlo simulations of a middle plane of  $56 \times 56 \times 5$  PZT supercells, where screening parameter  $\beta_s$  increases from 0.7250 to 0.8725 (with 0.025 increments).

summarizes the different resultant domain phases under different screening conditions at 300 K.

Next, we study the effect of changing ferroelectric layer thickness while keeping  $\beta_s$  fixed at 0.8. We also vary the external electric field to reveal if decreasing thickness facilitates the transitions toward short-circuit-like conditions, as the experiments indicate.

TABLE III. Domain phases observed under different screening conditions, i.e., various values of  $\beta_s$  at 300 K.

Screening condition	Domain phase
$\beta_s \leq 0.7125$	Striped/labyrinth
$0.7125 < \beta_s \leq 0.7850$	Disjoint striped/disjoint labyrinth
$0.7850 < \beta_s \leq 0.8125$	Bubble only
$\beta_s > 0.8125$	Monodomain

In this investigation, all studied films have  $56 \times 56$  supercell sized cross-sections, while the thickness varies from 4 to 10 u.c., and we extracted the external electric field vs PZT thickness phase diagram, as shown in Fig. 5(a) at 300 K. This figure demonstrates that, when decreasing such thickness, smaller external fields typically cause transition of the dipolar structure through the following phases, in the order (I) labyrinth, (II) broken labyrinth, (III) bubble-bimeron mixed, (IV) bubble only, and (V) monodomain/matrix [14] (note that, in the case of the film of 4 u.c., the system stays in a monodomain state). In other words, it is easier for thinner films to adopt short-circuit-like states, likely because of the role of surface dipoles. As a result, for a given value of external electric field, decreasing the thicknesses of PZT will result in various equilibrium dipolar structures, as illustrated by the dashed horizontal line, for an electric field of magnitude  $30 \times 10^7$  V/m, in Fig. 5(a). Figs. 5(b1)–5(b6) show snapshots of a middle [100]–[010] plane of PZT thickness ranging from 5 to 10 u.c. of the obtained variety of dipolar

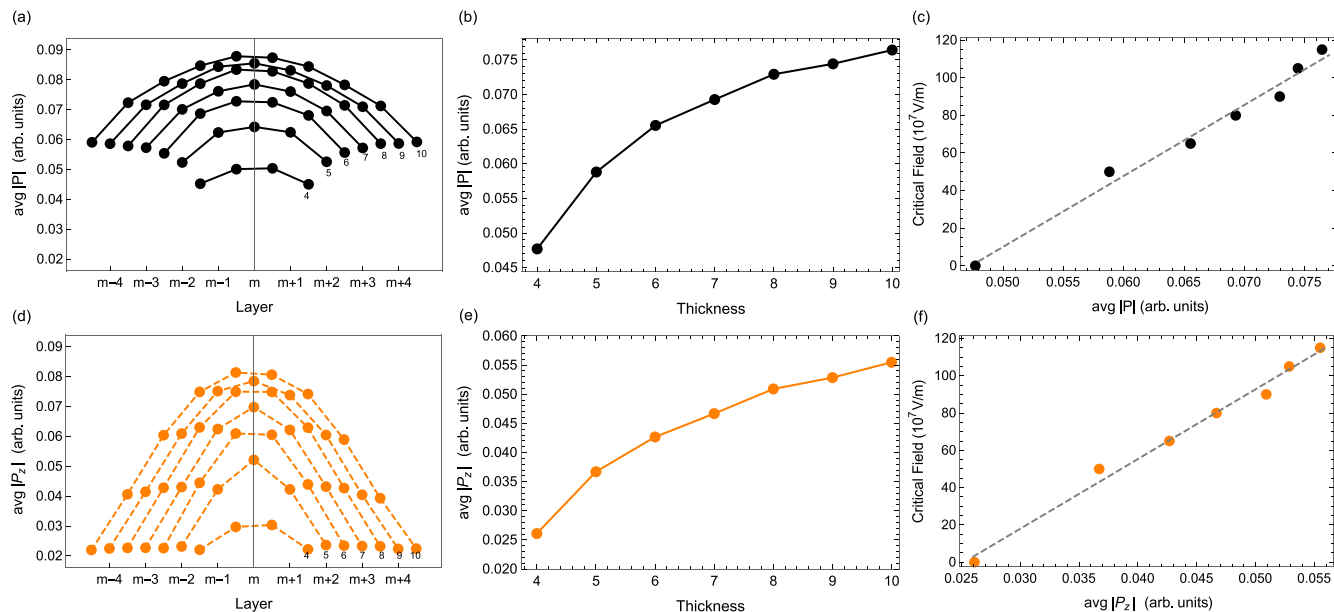


FIG. 6. (a) Average magnitude of polarization changes layer-by-layer for a labyrinthine state with no externally applied electric field. The supercell sizes considered are  $56 \times 56 \times Z$ , where  $Z$  varies from 4 to 10 layers (numbers 4 through 10 beside each curve indicates  $Z$ /thickness for that curve). Here,  $m$  is the  $z$  coordinate of the middle layer. (b) Plots of average magnitude of polarization vs supercell thickness, and (c) the critical external electric field required to transition to monodomain state differ as a function of average magnitude of polarization and  $z$  component of polarization. (d) Average magnitude of the  $z$  component of polarization of the labyrinthine state varies layer-by-layer. (e) Average magnitude of the  $z$  component of polarization varies with supercell thickness. (f) Critical external electric field required to transition to monodomain state as a function of average magnitude of the  $z$  component of polarization.

structures along the horizontal dashed line of Fig. 5(a). One can notice that, along this dashed horizontal line and as the thickness decreases, the following states progressively appear: connected labyrinth, broken labyrinth, bubble-bimeron mixed state, bubble only, and monodomain/matrix. One therefore goes from open-circuit-like to short-circuit-like states when the thickness decreases, in agreement with the experimental findings of the states found in S2-PZT9 vs S2-PZT8.

To further understand why Fig. 5 reveals that decreasing film thickness results in smaller critical external fields toward short-circuit-like states, we calculate the average magnitude of the polarization  $|P|$  and its  $z$  component  $|P_z|$  layer by layer in the labyrinth state adopted by films with various thicknesses, as shown in Figs. 6(a) and 6(d). These two figures tell us (1) these two magnitudes progressively increase as one goes from the surface to the inner layers, and (2) the surface layers contain significant in-plane dipoles (since  $|P_z|$  and  $|P|$  greatly differ at the surface layers) to close the flux. Consequently,  $|P_z|$  averaged over all layers decreases as the thickness is reduced, as demonstrated in Fig. 6(e). Moreover, Fig. 6(f) nicely shows that the critical field needed to induce a monodomain state is basically linear with this  $|P_z|$  averaged over all layers. One can then safely conclude that, as thickness decreases, the surface dipoles play an increasingly significant role that results in a decrease of the averaged  $|P_z|$  in the labyrinth states, which in turn facilitate the transition toward short-circuit-like states. Hence, the experimental observation of the breakdown of labyrinthine domains into finer domains upon decreasing the thickness of ferroelectric thin films can be explained in terms of the enhancement of surface effects with film thickness reduction.

#### IV. CONCLUSIONS

In summary, a gradual evolution of labyrinthine domains into nanoscale bubble domains has been observed in PZT/STO/PZT/LSMO//STO (001) ferroelectric heterostructures by varying film thicknesses of individual layers. Though change in thickness of each layer influences the depolarization field in a different manner, they all impel a domain morphology transformation which can be unfolded in a topological transition. The latter is attested by the observation of intermediary transitional states such as merons, skyrmions, dislocations, bimerons, and three- or four-fold junctions. This manipulation of topological transitions opens a window into using ferroelectric topologies in future nanoelectronics.

#### ACKNOWLEDGMENTS

The research at University of New South Wales was supported by DARPA Grant No. HR0011727183-D18AP00010 (TEE Program), partially supported by the Australian Research Council (ARC) Centre of Excellence (CoE) Future Low Energy Electronics (FLEET) CE170100039, and funded by the Australian Government Grant No. DP170102550. Q.Z. acknowledges the support of a Women in FLEET Fellowship. The research at University of Arkansas was also supported by the Vannevar Bush Faculty Fellowship Grant No. N00014-20-1-2834 from the Department of Defense and Arkansas Research Alliance.

The authors declare no conflict of interest.



- [1] N. D. Mermin, The topological theory of defects in ordered media, *Rev. Mod. Phys.* **51**, 591 (1979).
- [2] A. K. Yadav, C. T. Nelson, S. L. Hsu, Z. Hong, J. D. Clarkson, C. M. Schlepütz, A. R. Damodaran, P. Shafer, E. Arenholz, L. R. Dedon, D. Chen, A. Vishwanath, A. M. Minor, L. Q. Chen, J. F. Scott, L. W. Martin, and R. Ramesh, Observation of polar vortices in oxide superlattices, *Nature (London)* **530**, 198 (2016).
- [3] I. I. Naumov, L. Bellaïche, and H. Fu, Unusual phase transitions in ferroelectric nanodisks and nanorods, *Nature (London)* **432**, 737(2004).
- [4] Y. Nahas, S. Prokhorenko, and L. Bellaïche, Frustration and Self-Ordering of Topological Defects in Ferroelectrics, *Phys. Rev. Lett.* **116**, 117603 (2016).
- [5] J. Kim, M. You, K.-E. Kim, K. Chu, and C.-H. Yang, Artificial creation and separation of a single vortex-antivortex pair in a ferroelectric flatland, *npj Quantum Mater.* **4**, 292019 (2019).
- [6] Y. Li, Y. Jin, X. Lu, J.-C. Yang, Y.-H. Chu, F. Huang, J. Zhu, and S.-W. Cheong, Rewritable ferroelectric vortex pairs in BiFeO<sub>3</sub>, *npj Quantum Mater.* **2**, 43 (2017).
- [7] Y. Nahas, S. Prokhorenko, I. Kornev, and L. Bellaïche, Emergent Berezinskii-Kosterlitz-Thouless Phase in Low-Dimensional Ferroelectrics, *Phys. Rev. Lett.* **119**, 117601 (2017).
- [8] L. J. McGilly, A. Schilling, and J. M. Gregg, Domain bundle boundaries in single crystal BaTiO<sub>3</sub> lamellae: Searching for naturally forming dipole flux-closure/quadrupole chains, *Nano Lett.* **10**, 4200 (2010).
- [9] R. G. P. McQuaid, L. J. McGilly, P. Sharma, A. Gruverman, and J. M. Gregg, Mesoscale flux-closure domain formation in single-crystal BaTiO<sub>3</sub>, *Nat. Commun.* **2**, 404 (2011).
- [10] J. J. P. Peters, G. Apachitei, R. Beanland, M. Alexe, and A. M. Sanchez, Polarization curling and flux closures in multiferroic tunnel junctions, *Nat. Commun.* **7**, 13484 (2016).
- [11] Y. L. Tang, Y. L. Zhu, X. L. Ma, A. Y. Borisevich, A. N. Morozovska, E. A. Eliseev, W. Y. Wang, Y. J. Wang, Y. B. Xu, Z. D. Zhang, and S. J. Pennycook, Observation of a periodic array of flux-closure quadrants in strained ferroelectric PbTiO<sub>3</sub> films, *Science* **348**, 547 (2015).
- [12] S. Das, Y. L. Tang, Z. Hong, M. A. P. Gonçalves, M. R. McCarter, C. Klewe, K. X. Nguyen, F. Gómez-Ortiz, P. Shafer, E. Arenholz, V. A. Stoica, S.-L. Hsu, B. Wang, C. Ophus, J. F. Liu, C. T. Nelson, S. Saremi, B. Prasad, A. B. Mei, D. G. Schlom *et al.*, Observation of room-temperature polar skyrmions, *Nature (London)* **568**, 368 (2019).
- [13] Y. Nahas, S. Prokhorenko, L. Louis, Z. Gui, I. Kornev, and L. Bellaïche, Discovery of stable skyrmionic state in ferroelectric nanocomposites, *Nat. Commun.* **6**, 8542 (2015).
- [14] Y. Nahas, S. Prokhorenko, Q. Zhang, V. Govinden, N. Valanoor, and L. Bellaïche, Topology and control of self-assembled domain patterns in low-dimensional ferroelectrics, *Nat. Commun.* **11**, 8542 (2020).
- [15] L. Lu, Y. Nahas, M. Liu, H. Du, Z. Jiang, S. Ren, D. Wang, L. Jin, S. Prokhorenko, C.-L. Jia, and L. Bellaïche, Topological Defects with Distinct Dipole Configurations in PbTiO<sub>3</sub>/SrTiO<sub>3</sub> Multilayer Films, *Phys. Rev. Lett.* **120**, 177601 (2018).
- [16] D. Sichuga and L. Bellaïche, Epitaxial Pb(Zr, Ti)O<sub>3</sub> Ultrathin Films under Open-Circuit Electrical Boundary Conditions, *Phys. Rev. Lett.* **106**, 196102 (2011).
- [17] Q. Zhang, L. Xie, G. Liu, S. Prokhorenko, Y. Nahas, X. Pan, L. Bellaïche, A. Gruverman, and N. Valanoor, Nanoscale bubble domains and topological transitions in ultrathin ferroelectric films, *Adv. Mater.* **29**, 1702375 (2017).
- [18] B.-K. Lai, I. Ponomareva, I. I. Naumov, I. Kornev, H. Fu, L. Bellaïche, and G. J. Salamo, Electric-Field-Induced Domain Evolution in Ferroelectric Ultrathin Films, *Phys. Rev. Lett.* **96**, 137602 (2006).
- [19] Y. J. Wang, Y. P. Feng, Y. L. Zhu, Y. L. Tang, L. X. Yang, M. J. Zou, W. R. Geng, M. J. Han, X. W. Guo, B. Wu, and X. L. Ma, Polar meron lattice in strained oxide ferroelectrics, *Nat. Mater.* **19**, 881 (2020).
- [20] Y. Nahas, S. Prokhorenko, J. Fischer, J. B. Xu, C. Carrétéro, S. Prosandeev, M. Bibes, S. Fusil, B. Dkhil, V. Garcia, and L. Bellaïche, Inverse transition of labyrinthine domain patterns in ferroelectric thin films, *Nature (London)* **577**, 47 (2020).
- [21] S. Prokhorenko, Y. Nahas, and L. Bellaïche, Fluctuations and Topological Defects in Proper Ferroelectric Crystals, *Phys. Rev. Lett.* **118**, 147601 (2017).
- [22] Y. Nahas, S. Prokhorenko, I. Kornev, and L. Bellaïche, Topological Point Defects in Relaxor Ferroelectrics, *Phys. Rev. Lett.* **116**, 127601 (2016).
- [23] S. Prosandeev, S. Prokhorenko, Y. Nahas, and L. Bellaïche, Prediction of a novel topological multidefect ground state, *Phys. Rev. B* **100**, 140104 (2019).
- [24] A. R. Damodaran, J. D. Clarkson, Z. Hong, H. Liu, A. K. Yadav, C. T. Nelson, S.-L. Hsu, M. R. McCarter, K.-D. Park, V. Kravtsov, A. Farhan, Y. Dong, Z. Cai, H. Zhou, P. Aguado-Puente, P. García-Fernández, J. Íñiguez, J. Junquera, A. Scholl, M. B. Raschke *et al.*, Phase coexistence and electric-field control of toroidal order in oxide superlattices, *Nat. Mater.* **16**, 1003 (2017).
- [25] S. Prosandeev, A. Malashevich, Z. Gui, L. Louis, R. Walter, I. Souza, and L. Bellaïche, Natural optical activity and its control by electric field in electrotoroidic systems, *Phys. Rev. B* **87**, 195111 (2013).
- [26] P. Shafer, P. García-Fernández, P. Aguado-Puente, A. R. Damodaran, A. K. Yadav, C. T. Nelson, S. L. Hsu, J. C. Wojdeł, J. Íñiguez, L. W. Martin, E. Arenholz, J. Junquera, and R. Ramesh, Emergent chirality in the electric polarization texture of titanate superlattices, *Proc. Natl. Acad. Sci. USA* **115**, 915 (2018).
- [27] A. K. Yadav, K. X. Nguyen, Z. Hong, P. García-Fernández, P. Aguado-Puente, C. T. Nelson, S. Das, B. Prasad, D. Kwon, S. Cheema, A. I. Khan, C. Hu, J. Íñiguez, J. Junquera, L.-Q. Chen, D. A. Muller, R. Ramesh, and S. Salahuddin, Spatially resolved steady-state negative capacitance, *Nature (London)* **565**, 468 (2019).
- [28] N. Balke, B. Winchester, W. Ren, Y. H. Chu, A. N. Morozovska, E. A. Eliseev, M. Huijben, R. K. Vasudevan, P. Maksymovych, J. Britson, S. Jesse, I. Kornev, R. Ramesh, L. Bellaïche, L. Q. Chen, and S. V. Kalinin, Enhanced electric conductivity at ferroelectric vortex cores in BiFeO<sub>3</sub>, *Nat. Phys.* **8**, 81 (2012).
- [29] I. Kornev, H. Fu, and L. Bellaïche, Ultrathin Films of Ferroelectric Solid Solutions under a Residual Depolarizing Field, *Phys. Rev. Lett.* **93**, 196104 (2004).
- [30] V. Nagarajan, I. G. Jenkins, S. P. Alpay, H. Li, S. Aggarwal, L. Salamanca-Riba, A. L. Roytburd, and R. Ramesh, Thickness dependence of structural and electrical properties in epitaxial lead zirconate titanate films, *J. Appl. Phys.* **86**, 595 (1999).

- [31] D. Sando, A. Barthélémy, and M. Bibes, BiFeO<sub>3</sub> epitaxial thin films and devices: Past, present and future, *J. Condens. Matter Phys.* **26**, 473201 (2014).
- [32] J. M. Bursian and O. I. Zaikovskii, Changes in curvature of a ferroelectric film due to polarization, *Sov. Phys.-Solid State* **10**, 1121 (1968).
- [33] S. M. Kogan, Piezoelectric effect during inhomogeneous deformation and acoustic scattering of carriers in crystals, *Sov. Phys. Solid State* **5**, 2069 (1964).
- [34] L. E. Cross, Flexoelectric effects: Charge separation in insulating solids subjected to elastic strain gradients, *J. Mater. Sci.* **41**, 53 (2006).
- [35] J. Hong, G. Catalan, J. F. Scott, and E. Artacho, The flexoelectricity of barium and strontium titanates from first principles, *J. Phys. Condens. Matter* **22**, 112201 (2010).
- [36] A. Gruverman, B. J. Rodriguez, A. I. Kingon, R. J. Nemanich, A. K. Tagantsev, J. S. Cross, and M. Tsukada, Mechanical stress effect on imprint behavior of integrated ferroelectric capacitors, *Appl. Phys. Lett.* **83**, 728 (2003).
- [37] H. Pöttker and E. K. H. Salje, Flexoelectricity, incommensurate phases and the Lifshitz point, *J. Phys. Condens. Matter* **28**, 075902 (2016).
- [38] M. Dawber, P. Chandra, P. B. Littlewood, and J. F. Scott, Depolarization corrections to the coercive field in thin-film ferroelectrics, *J. Phys. Condens. Matter* **15**, L393 (2003).
- [39] M. Dawber, N. Stucki, C. Lichtensteiger, S. Gariglio, and J.-M. Triscone, New phenomena at the interfaces of very thin ferroelectric oxides, *J. Phys. Condens. Matter* **20**, 264015 (2008).
- [40] R. R. Mehta, B. D. Silverman, and J. T. Jacobs, Depolarization fields in thin ferroelectric films, *J. Appl. Phys.* **44**, 3379 (1973).
- [41] C. Lichtensteiger, S. Fernandez-Pena, C. Weymann, P. Zubko, and J.-M. Triscone, Tuning of the depolarization field and nanodomain structure in ferroelectric thin films, *Nano Lett.* **14**, 4205 (2014).
- [42] G. Liu, J. Chen, C. Lichtensteiger, J.-M. Triscone, P. Aguado-Puente, J. Junquera, and N. Valanoor, Positive effect of an internal depolarization field in ultrathin epitaxial ferroelectric films, *Adv. Electron. Mater.* **2**, 1500288 (2016).
- [43] S. Lisenkov and L. Bellaiche, Phase diagrams of BaTiO<sub>3</sub>/SrTiO<sub>3</sub> superlattices from first principles, *Phys. Rev. B* **76**, 020102 (2007).
- [44] J. Junquera and P. Ghosez, Critical thickness for ferroelectricity in perovskite ultrathin films, *Nature (London)* **422**, 506 (2003).
- [45] V. Govinden, Q. Zhang, D. Sando, and N. Valanoor, Depolarization field tuning of nanoscale ferroelectric domains in (001), PbZr<sub>0.4</sub>Ti<sub>0.6</sub>O<sub>3</sub>/SrTiO<sub>3</sub>/PbZr<sub>0.4</sub>Ti<sub>0.6</sub>O<sub>3</sub> epitaxial heterostructures, *J. Appl. Phys.* **129**, 024104 (2021).
- [46] E. A. Eliseev, Y. M. Fomichov, S. V. Kalinin, Y. M. Vysochanskii, P. Maksymovich, and A. N. Morozovska, Labyrinthine domains in ferroelectric nanoparticles: Manifestation of a gradient-induced morphological transition, *Phys. Rev. B* **98**, 054101 (2018).
- [47] L. Bellaiche, A. García, and D. Vanderbilt, Finite-Temperature Properties of Pb(Zr<sub>1-x</sub>Ti<sub>x</sub>)O<sub>3</sub> Alloys from First Principles, *Phys. Rev. Lett.* **84**, 5427 (2000).
- [48] I. Ponomareva, I. I. Naumov, I. Kornev, H. Fu, and L. Bellaiche, Atomistic treatment of depolarizing energy and field in ferroelectric nanostructures, *Phys. Rev. B* **72**, 140102 (2005).
- [49] T. Ohnishi, H. Koinuma, and M. Lippmaa, Pulsed laser deposition of oxide thin films, *Appl. Surf. Sci.* **252**, 2466 (2006).
- [50] C. Yu, A. S. Sokolov, P. Kulik, and V. G. Harris, Stoichiometry, phase, and texture evolution in PLD-grown hexagonal barium ferrite films as a function of laser process parameters, *J. Alloys Compd.* **814**, 152301 (2020).
- [51] C. Lichtensteiger, INTERACTIVEXRFIT: A new tool to simulate and fit X-ray diffractograms of oxide thin films and heterostructures, *J. Appl. Crystallogr.* **51**, 1745 (2018).
- [52] See Supplemental Material at <http://link.aps.org/supplemental/10.1103/PhysRevMaterials.5.124205> for more details on the structural analysis; phase image of sample F2(S2-PZT9); an investigation of the effects of thickness and screening parameter variation at 10 K; and experimental evidence of the domain transition when only thickness of ferroelectric layer is varied.
- [53] I. M. Dildar, C. Beekman, X. He, and J. Aarts, Hall effect measurements on strained and unstrained thin films of La<sub>0.7</sub>Ca<sub>0.3</sub>MnO<sub>3</sub> and La<sub>0.7</sub>Sr<sub>0.3</sub>MnO<sub>3</sub>, *Phys. Rev. B* **85**, 205103 (2012).
- [54] M. Adachi, Y. Akishige, T. Asahi, K. Deguchi, K. Gesi, K. Hasebe, T. Hikita, T. Ikeda, Y. Iwata, M. Komukae, T. Mitsui, E. Nakamura, N. Nakatani, M. Okuyama, T. Osaka, A. Sakai, E. Sawaguchi, Y. Shiozaki, T. Takenaka, K. Toyoda, T. Tsukamoto, and T. Yagi, in *Landolt-Börnstein - Group III Condensed Matter 36A1*, edited by Y. Shiozaki, E. Nakamura, and T. Mitsui (Springer, 2001).
- [55] G. Catalan, B. Noheda, J. McAneney, L. J. Sinnamon, and J. M. Gregg, Strain gradients in epitaxial ferroelectrics, *Phys. Rev. B* **72**, 020102 (2005).
- [56] S. K. Streiffer, J. A. Eastman, D. D. Fong, C. Thompson, A. Munkholm, M. V. R. Murty, O. Auciello, G. R. Bai, and G. B. Stephenson, Observation of Nanoscale 180° Stripe Domains in Ferroelectric PbTiO<sub>3</sub> Thin Films, *Phys. Rev. Lett.* **89**, 067601 (2002).
- [57] M.-B. Lepetit, B. Mercey, and C. Simon, Interface Effects in Perovskite Thin Films, *Phys. Rev. Lett.* **108**, 087202 (2012).
- [58] C. G. Callan Jr, R. Dashen, and D. J. Gross, Toward a theory of the strong interactions, *Phys. Rev. D* **17**, 2717 (1978).